Available online at www.sciencedirect.com
SCIENCE DIRECT
ELSEVIER
Thin-Walled Structures 43 (2005) 1615–1645
THIN-WALLED STRUCTURES
www.elsevier.com/locate/tws

Non-linear model for stability of thin-walled composite beams with shear deformation

Sebastián P. Machado[a,b], Víctor H. Cortínez[a,b,*]

[a]*Grupo Análisis de Sistemas Mecánicos, Facultad Regional Bahía Blanca, Universidad Tecnológica Nacional, 11 de abril 461, B8000LMI Bahía Blanca, Argentina*
[b]*CONICET, Argentina*

Received 12 April 2005; received in revised form 16 May 2005; accepted 6 June 2005
Available online 18 August 2005

Abstract

A geometrically non-linear theory for thin-walled composite beams is developed for both open and closed cross-sections and taking into account shear flexibility (bending and warping shear). This non-linear formulation is used for analyzing the static stability of beams made of composite materials subjected to concentrated end moments, concentrated forces, or uniformly distributed loads. Composite is assumed to be made of symmetric balanced laminates or especially orthotropic laminates. In order to solve the non-linear differential system, Ritz's method is first applied. Then, the resulting algebraic equilibrium equations are solved by means of an incremental Newton–Rapshon method. This paper investigates numerically the flexural–torsional and lateral buckling and post-buckling behavior of simply supported beams, pointing out the influence of shear–deformation for different laminate stacking sequence and the pre-buckling deflections effect on buckling loads. The numerical results show that the classical predictions of lateral buckling are conservative when the pre-buckling displacements are not negligible, and a non-linear buckling analysis may be required for reliable solutions.

Keywords: Thin-walled beams; Shear flexibility; Composite; Non-linear theory; Post-buckling

* Corresponding author. Address: Grupo Análisis de Sistemas Mecánicos, Facultad Regional Bahía Blanca, Universidad Tecnológica Nacional, 11 de abril 461, B8000LMI Bahía Blanca, Argentina. Tel.: +54 291 4555220; fax: +54 291 4555311.
E-mail address: vcortine@frbb.utn.edu.ar (V.H. Cortínez).

0263-8231/$ - see front matter © 2005 Elsevier Ltd. All rights reserved.
doi:10.1016/j.tws.2005.06.008

1. Introduction

Structural members made of composites are increasingly used in aeronautical, mechanical and civil engineering applications, where high strength and stiffness, and low weight are of primary importance. Many structural members made of composites have the form of thin-walled beams. The load carrying capacity of this kind of members is often governed by instability. Thin-walled beams may fail in a flexural or/and torsional buckling mode: the beam suddenly deflects laterally or twists out of the plane of loading. The buckling of the beam is caused by the coupling among bending, twisting and stretching deformations. For this reason, a non-linear theory is required for the accurate behavior prediction of such structures. The limitation of the linear buckling analysis of beam problems [1] is the omission of any consideration of the effect of pre-buckling deflections of the beam. This omission is not important when the pre-buckling deflection of the beam is negligible. In other cases, however, the effect of the pre-buckling deflections must be taken into account for obtaining accurate predictions of buckling loads. For example, lateral buckling is a relevant phenomenon [2] that, in particular, involves mechanical complications, since structures may experience large or moderately large deflections and rotations before buckling occurs. Moreover, the linear buckling gives no information about the shape of the secondary path of equilibrium (post-buckling). Sometimes the behavior of a structure can be understood only if the shape of the secondary path is known. Thus, the additional load carrying capacity after buckling can be determined.

Keeping in mind the importance of the problem, a significant amount of research has been conduced in recent years toward the development of non-linear theories of three-dimensional beams. Most of these have been confined to metallic structures [3–7], for example]. On the other hand, the amount of work carried out on thin-walled beams made of composite materials has been rather limited. Bhaskar and Librescu [8] presented a geometrically non-linear theory for thin-walled composite beams, but post-buckling analyzes were not performed. The non-linear stability analysis of thin-walled composite beams with open cross-section has been recently investigated by Fraternali and Feo [9] using a finite element formulation and without considering shear–deformation.

The objective of this paper is to investigate the post-buckling behavior and the effect of pre-buckling deflections on the buckling loads of thin-walled composite beams using a geometrically non-linear beam theory, for both open and closed cross-sections and taking into account several non-classical effects. On the other hand, it is valid for symmetric balanced laminates and especially orthotropic laminates [10]. As a distinctive feature, the present beam model incorporates, in a full form, the effects of shear flexibility (bending and warping shear). This shear effect plays an important role in the analysis of linear stability of thin-walled composite beams [11–14]. In this paper, the non-linear model is used to predict the post-buckling behavior of simply supported thin-walled composite beams subjected to different load conditions. This work is basically divided into two kinds of analysis. First, the flexural–torsional post-buckling of beams subjected to a compression load is studied for different cross-sectional shapes. Then, beams with uniform bending moments, concentrated forces, or uniformly distributed load are considered to investigate the lateral buckling and post-buckling behavior. In all the cases, the influence of shear–deformation is analyzed for different laminate stacking sequences.

2. Kinematics

A straight thin-walled composite beam with an arbitrary cross-section is considered (Fig. 1). The points of the structural member are referred to a Cartesian co-ordinate system $(x, \bar{y}, \bar{z})$, where the x-axis is parallel to the longitudinal axis of the beam while $\bar{y}$ and $\bar{z}$ are the principal axes of the cross-section. The axes-y and -z are parallel to the principal ones but having their origin at the shear center (defined according to Vlasov's theory of isotropic beams). The co-ordinates corresponding to points lying on the middle line are denoted as Y and Z (or $\bar{Y}$ and $\bar{Z}$). In addition, a circumferential co-ordinate s and a normal co-ordinate n are introduced on the middle contour of the cross-section:

$$\bar{y}(s,n) = \bar{Y}(s) - n\frac{\mathrm{d}Z}{\mathrm{d}s}, \qquad \bar{z}(s,n) = \bar{Z}(s) + n\frac{\mathrm{d}Y}{\mathrm{d}s} \tag{1}$$

$$y(s,n) = Y(s) - n\frac{\mathrm{d}Z}{\mathrm{d}s}, \qquad z(s,n) = Z(s) + n\frac{\mathrm{d}Y}{\mathrm{d}s} \tag{2}$$

On the other hand, y_0 and z_0 are the centroidal co-ordinates measured with respect to the shear center:

$$\bar{y}(s,n) = y(s,n) - y_0 \qquad \bar{z}(s,n) = z(s,n) - z_0 \tag{3}$$

The present structural model is based on the following assumptions [13]:

(1) The cross-section contour is rigid in its own plane.
(2) The warping distribution is assumed to be given by the Saint–Venant function for isotropic beams.
(3) Flexural rotations (about the $\bar{y}$- and $\bar{z}$-axes) are assumed to be moderate, while the twist ϕ of the cross-section can be arbitrarily large.
(4) Shell force and moment resultant corresponding to the circumferential stress σ_{ss} and the force resultant corresponding to γ_{ns} are neglected.

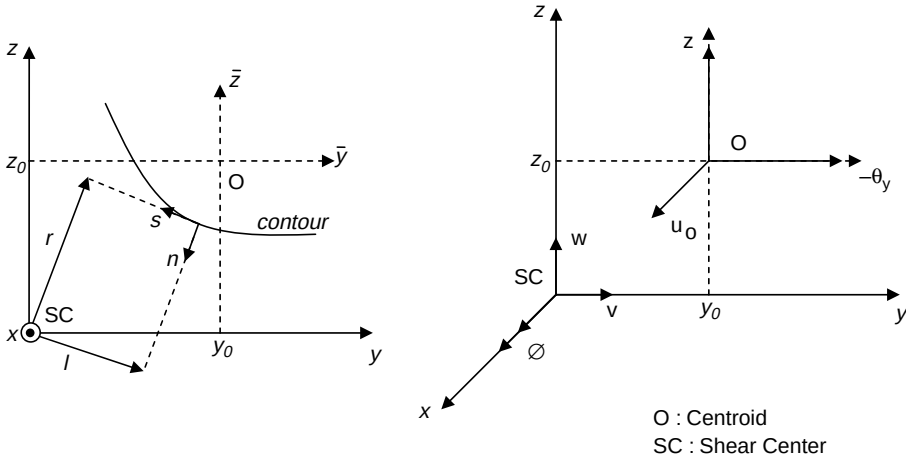

Fig. 1. Co-ordinate system of the cross-section and notation for displacement measures.

(5) The radius of curvature at any point of the shell is neglected.
(6) Twisting linear curvature of the shell is expressed according to the classical plate theory.
(7) The laminate stacking sequence is assumed to be symmetric and balanced, or especially orthotropic [10].

According to these hypotheses, the displacement field is assumed to be in the following form:

$$\begin{aligned} u_x &= u_0 - \bar{y}(\theta_z \cos\phi + \theta_y \sin\phi) - \bar{z}(\theta_y \cos\phi - \theta_z \sin\phi) \\ &\quad + \omega\left[\theta - \underline{\frac{1}{2}(\theta_y'\theta_z - \theta_y\theta_y')}\right] + (\theta_z z_0 - \theta_y y_0)\sin\phi \\ u_y &= v - z\sin\phi - y(1-\cos\phi) - \underline{\frac{1}{2}(\theta_z^2\bar{y} + \theta_z\theta_y\bar{z})} \\ u_z &= w + y\sin\phi - z(1-\cos\phi) - \underline{\frac{1}{2}(\theta_y^2\bar{z} + \theta_z\theta_y\bar{y})} \end{aligned} \tag{4}$$

This expression is a generalization of others previously proposed in the literature.

The displacement field proposed by Fraternali and Feo [9] is recovered (see Appendix A) by considering $\theta_z = v'$, $\theta_y = w'$ and $\theta = \phi'$ (neglecting flexural and torsional shear flexibility), approximating $\cos\phi$ and $\sin\phi$ by $(1-\phi^2/2)$ and ϕ, respectively, and conserving non-linear terms up to second-order. Moreover, the displacement field of the classical Vlasov theory is obtained when second-order effects are ignored.

On the other hand, a simplified analog of Eq. (4), disregarding the underlined terms and shear flexibility, was used by Mohri [6].

As a final comparison, taking $\cos\phi = 1$ and $\sin\phi = \phi$ and disregarding the non-linear terms, the displacement field (4) coincides with the one formulated by Cortínez and Piovan [13] for linear dynamics of shear–deformable thin-walled beams.

In the above expressions, ϕ, θ_y and θ_z are measures of the rotations about the shear center axis, $\bar{y}$- and $\bar{z}$-axes, respectively; θ represents the warping variable of the cross-section. Furthermore, the superscript 'prime' denotes derivation with respect to the variable x. The warping function ω of the thin-walled cross-section may be defined as

$$\omega(s,n) = \omega_{\mathrm{p}}(s) + \omega_{\mathrm{s}}(s,n) \tag{5}$$

where ω_{p} and ω_{s} are the contour warping function and the thickness warping function, respectively. They are defined in the form [15]

$$\omega_{\mathrm{p}}(s) = \frac{1}{S}\left[\int_0^S \left(\int_{s_0}^s [r(s) - \psi(s)]\mathrm{d}s\right)\mathrm{d}s\right] - \int_{s_0}^s [r(s) - \psi(s)]\mathrm{d}s \qquad \omega_{\mathrm{s}}(s,n) = -nl(s) \tag{6}$$

where

$$r(s) = -Z(s)\frac{\mathrm{d}Y}{\mathrm{d}s} + Y(s)\frac{\mathrm{d}Z}{\mathrm{d}s} \tag{7}$$

$$l(s) = Y(s)\frac{\mathrm{d}Y}{\mathrm{d}s} + Z(s)\frac{\mathrm{d}Z}{\mathrm{d}s} \tag{8}$$

$r(s)$ represents the perpendicular distance from the shear center (SC) to the tangent at any point of the mid-surface contour, and $l(s)$ represents the perpendicular distance from the shear center (SC) to the normal at any point of the mid-surface contour, as shown in Fig. 1.

In the expression (6), Ψ is the shear strain at the middle line, obtained by means of the Saint–Venant theory of pure torsion for isotropic beams, and normalized with respect to $\mathrm{d}\phi/\mathrm{d}x$ [16]. For the case of open sections, $\Psi = 0$.

3. The strain field

The displacements with respect to the curvilinear system (x,s,n) are obtained by means of the following expressions:

$$\bar{U} = u_x(x,s,n) \tag{9}$$

$$\bar{V} = u_y(x,s,n)\frac{\mathrm{d}Y}{\mathrm{d}s} + u_z(x,s,n)\frac{\mathrm{d}Z}{\mathrm{d}s} \tag{10}$$

$$\bar{W} = -u_y(x,s,n)\frac{\mathrm{d}Z}{\mathrm{d}s} + u_z(x,s,n)\frac{\mathrm{d}Y}{\mathrm{d}s} \tag{11}$$

The three non-zero components ε_{xx}, ε_{xs}, ε_{xn} of the Green's strain tensor are given by:

$$\varepsilon_{xx} = \frac{\partial \bar{U}}{\partial x} + \frac{1}{2}\left[\left(\frac{\partial \bar{U}}{\partial x}\right)^2 + \left(\frac{\partial \bar{V}}{\partial x}\right)^2 + \left(\frac{\partial \bar{W}}{\partial x}\right)^2\right] \tag{12}$$

$$\varepsilon_{xs} = \frac{1}{2}\left[\frac{\partial \bar{U}}{\partial s} + \frac{\partial \bar{V}}{\partial x} + \frac{\partial \bar{U}}{\partial x}\frac{\partial \bar{U}}{\partial s} + \frac{\partial \bar{V}}{\partial x}\frac{\partial \bar{V}}{\partial s} + \frac{\partial \bar{W}}{\partial x}\frac{\partial \bar{W}}{\partial s}\right] \tag{13}$$

$$\varepsilon_{xn} = \frac{1}{2}\left[\frac{\partial \bar{U}}{\partial n} + \frac{\partial \bar{W}}{\partial x} + \frac{\partial \bar{U}}{\partial x}\frac{\partial \bar{U}}{\partial n} + \frac{\partial \overline{V}}{\partial x}\frac{\partial \overline{V}}{\partial n} + \frac{\partial \bar{W}}{\partial x}\frac{\partial \bar{W}}{\partial n}\right] \tag{14}$$

Substituting expressions (4) into (9)–(11) and then into (12)–(14), employing the relations (1)–(3) and (5)–(8), one obtains after simplifying some higher order terms, the components of the strain tensor which can be expressed in the following form

$$\varepsilon_{xx} = \varepsilon_{xx}^{(0)} + n\kappa_{xx}^{(1)} \qquad \gamma_{xs} = 2\varepsilon_{xs} = \gamma_{xs}^{(0)} + n\kappa_{xs}^{(1)} \qquad \gamma_{xn} = 2\varepsilon_{xn} = \gamma_{xn}^{(0)} \tag{15}$$

where

$$\varepsilon_{xx}^{(0)} = u_0' + \frac{1}{2}(u_0'^2 + v'^2 + w'^2) + \omega_{\mathrm{p}}\left[\theta' - \frac{1}{2}(\theta_z\theta_y'' - \theta_y\theta_z'')\right] + \bar{Z}[(-\theta_y' - u_0'\theta_y')\cos\phi + (\theta_z' + u_0'\theta_z')\sin\phi] + \bar{Y}[(-\theta_z' - u_0'\theta_z')\cos\phi - (\theta_y' + u_0'\theta_y')\sin\phi] + \frac{1}{2}\phi'^2(Y^2 + Z^2) + \frac{1}{2}\theta_y'^2\bar{Z}^2 + \frac{1}{2}\theta_z'^2\bar{Y}^2 + \theta_z'\theta_y'\bar{Z}\bar{Y} + (z_0\theta_z' - y_0\theta_y')\sin\phi + \phi'(z_0\theta_z - y_0\theta_y)\cos\phi \tag{16}$$

$$\kappa_{xx}^{(1)} = -\frac{\mathrm{d}Z}{\mathrm{d}s}[-(\theta_z' + u_0'\theta_z')\cos\phi - (\theta_y' + u_0'\theta_y')\sin\phi] + \frac{\mathrm{d}Y}{\mathrm{d}s}[(-\theta_y' - u_0'\theta_y')\cos\phi + (\theta_z' + u_0'\theta_z')\sin\phi] - l\left[\theta' - \frac{1}{2}(\theta_z\theta_y'' - \theta_y\theta_z'')\right] - r\phi'^2 - \bar{Y}\frac{\mathrm{d}Z}{\mathrm{d}s}\theta_z'^2 + \overline{Z}\frac{\mathrm{d}Y}{\mathrm{d}s}\theta_y'^2 + \left(\bar{Y}\frac{\mathrm{d}Y}{\mathrm{d}s} - \bar{Z}\frac{\mathrm{d}Z}{\mathrm{d}s}\right)\theta_y'\theta_z' \tag{17}$$

$$\gamma_{xs}^{(0)} = \frac{\mathrm{d}Y}{\mathrm{d}s}\left[(v' - \theta_z - u_0'\theta_z)\cos\phi - z_0\frac{1}{2}(\theta_z\theta_y' - \theta_y\theta_z') + (w' - \theta_y - u_0'\theta_y)\sin\phi\right] + (r - \psi)(\phi' - \theta) + \frac{\mathrm{d}Z}{\mathrm{d}s}\left[(w' - \theta_y - u_0'\theta_y)\cos\phi + y_0\frac{1}{2}(\theta_z\theta_y' - \theta_y\theta_z') - (v' - \theta_z - u_0'\theta_z)\sin\phi\right] + \psi\left[\phi' - \frac{1}{2}(\theta_z\theta_y' - \theta_y\theta_z')\right] \tag{18}$$

$$\kappa_{xs}^{(1)} = -2\left[\phi' - \frac{1}{2}(\theta_z\theta_y' - \theta_y\theta_z')\right] \tag{19}$$

$$\gamma_{xn}^{(0)} = \frac{\mathrm{d}Y}{\mathrm{d}s}\left[(w' - \theta_y - u_0'\theta_y)\cos\phi + y_0\frac{1}{2}(\theta_z\theta_y' - \theta_y\theta_z') - (v' - \theta_z - u_0'\theta_z)\sin\phi\right] - \frac{\mathrm{d}Z}{\mathrm{d}s}\left[(v' - \theta_z - u_0'\theta_z)\cos\phi - z_0\frac{1}{2}(\theta_z\theta_y' - \theta_y\theta_z') + (w' - \theta_y - u_0'\theta_y)\sin\phi\right] + l(\phi' - \theta) \tag{20}$$

4. Variational formulation

Taking into account the adopted assumptions, the principle of virtual work for a composite shell may be expressed in the form [13,17]

$$\begin{aligned}&\iint(N_{xx}\delta\varepsilon_{xx}^{(0)}+M_{xx}\delta\kappa_{xx}^{(1)}+N_{xs}\delta\gamma_{xs}^{(0)}+M_{xs}\delta\kappa_{xs}^{(1)}+N_{xn}\delta\gamma_{ns}^{(0)})\mathrm{d}s\mathrm{d}x\\&-\iint(\bar{q}_x\delta\bar{u}_x+\bar{q}_y\delta\bar{u}_y+\bar{q}_z\delta\bar{u}_z)\mathrm{d}s\mathrm{d}x-\iint(\bar{p}_x\delta u_x+\bar{p}_y\delta u_y+\bar{p}_z\delta u_z)\Big|_{x=0}\mathrm{d}s\mathrm{d}n\\&-\iint(\bar{p}_x\delta u_x+\bar{p}_y\delta u_y+\bar{p}_z\delta u_z)\Big|_{x=L}\mathrm{d}s\mathrm{d}n-\iiint(\bar{f}_x\delta u_x+\bar{f}_y\delta u_y+\bar{f}_z\delta u_z)\mathrm{d}s\mathrm{d}n\mathrm{d}x=0\end{aligned}\tag{21}$$

where N_{xx}, N_{xs}, M_{xx}, M_{xs} and N_{xn} are the shell stress resultants defined according to the following expressions:

$$\begin{aligned}&N_{xx}=\int_{-e/2}^{e/2}\sigma_{xx}\,\mathrm{d}n;\qquad M_{xx}=\int_{-e/2}^{e/2}(\sigma_{xx}n)\mathrm{d}n;\qquad N_{xs}=\int_{-e/2}^{e/2}\sigma_{xs}\,\mathrm{d}n;\\&M_{xs}=\int_{-e/2}^{e/2}(\sigma_{xs}n)\mathrm{d}n;\qquad N_{xn}=\int_{-e/2}^{e/2}\sigma_{xn}\,\mathrm{d}n\end{aligned}\tag{22}$$

The beam is subjected to wall surface tractions $\bar{q}_x$, $\bar{q}_y$ and $\bar{q}_z$ specified per unit area of the undeformed middle surface and acting along the x-, y- and z-directions, respectively. Similarly, $\bar{p}_x$, $\bar{p}_y$ and $\bar{p}_z$ are the end tractions per unit area of the undeformed cross-section specified at $x=0$ and $x=L$, where L is the undeformed length of the beam. Besides, $\bar{f}_x$, $\bar{f}_y$ and $\bar{f}_z$ are the body forces per unit of volume. Finally, denoting $\bar{u}_x$, $\bar{u}_y$ and $\bar{u}_z$ as displacements at the middle line.

5. Constitutive equations

The constitutive equations of symmetrically balanced laminates may be expressed in the terms of shell stress resultants in the following form [10]

$$\begin{Bmatrix}N_{xx}\\N_{xs}\\N_{xn}\\M_{xx}\\M_{xs}\end{Bmatrix}=\begin{bmatrix}\bar{A}_{11}&0&0&0&0\\0&\bar{A}_{66}&0&0&0\\0&0&\bar{A}_{55}^{(H)}&0&0\\0&0&0&\bar{D}_{11}&0\\0&0&0&0&\bar{D}_{66}\end{bmatrix}\begin{Bmatrix}\varepsilon_{xx}^{(0)}\\\gamma_{xs}^{(0)}\\\gamma_{xn}^{(0)}\\\kappa_{xx}^{(1)}\\\kappa_{xs}^{(1)}\end{Bmatrix}\tag{23}$$

with

$$\bar{A}_{11} = A_{11} - \frac{A_{12}^2}{A_{22}}, \qquad \bar{A}_{66} = A_{66} - \frac{A_{26}^2}{A_{22}}, \qquad \bar{A}_{55}^{(H)} = A_{55}^{(H)} - \frac{(A_{45}^{(H)})^2}{A_{44}^{(H)}}$$
$$\bar{D}_{11} = D_{11} - \frac{D_{12}^2}{D_{22}}, \qquad \bar{D}_{66} = D_{66} - \frac{D_{26}^2}{D_{22}} \tag{24}$$

where A_{ij}, D_{ij} and $A_{ij}^{(H)}$ are plate stiffness coefficients defined according to the lamination theory presented by Barbero [10]. The coefficient $\bar{D}_{16}$ has been neglected because of its low value for the considered laminate stacking sequence [13].

6. Governing equation

Substituting expressions (16)–(20) into (21) and integrating with respect to s, one obtains the one-dimensional expression for the virtual work equation given by

$$L_K + L_P = 0 \tag{25}$$

where L_k and L_p represent the virtual work contributions due to the internal and external forces, respectively. The corresponding expressions are given below

$$\begin{aligned}
L_K = \int_0^L \Big\{ & \delta u_0'[N + u_0' N - M_z(\theta_z' \cos\phi + \theta_y' \sin\phi) - M_y(\theta_y' \cos\phi + \theta_z' \sin\phi) \\
& - Q_y(\theta_z \cos\phi + \theta_y \sin\phi) - Q_z(\theta_y \cos\phi + \theta_z \sin\phi)] \\
& + \delta v'(Q_y \cos\phi - Q_z \sin\phi + v' N) + \delta w'(Q_z \cos\phi + Q_y \sin\phi + w' N) \\
& + \delta\theta_z \Big[-Q_y(1+u_0')\cos\phi + Q_z(1+u_0')\sin\phi + \frac{1}{2}(Q_z y_0 - Q_y z_0)\theta_y' - \frac{1}{2} T_{sv}\theta_y' \\
& - \frac{1}{2} B\theta_y'' + N\phi' z_0 \cos\phi \Big] + \delta\theta_z' \big[-M_z(1+u_0')\cos\phi + \theta_z' P_{zz} + \theta_y' P_{yz} \\
& + N z_0 \sin\phi + M_y(1+u_0')\sin\phi + \frac{1}{2}(Q_y z_0 - Q_z y_0)\theta_y + \frac{1}{2} T_{sv}\theta_y \Big] \\
& + \delta\theta_y \Big[\frac{1}{2} B\theta_z'' - N\phi' y_0 \cos\phi - Q_z(1+u_0')\cos\phi - Q_y(1+u_0')\sin\phi \\
& + \frac{1}{2}(Q_y z_0 - Q_z y_0)\theta_z' + \frac{1}{2} T_{sv}\theta_z' \Big] + \delta\theta_y' \big[-M_y(1+u_0')\cos\phi - M_z(1+u_0')\sin\phi \\
& - N y_0 \sin\phi + \frac{1}{2}(Q_z y_0 - Q_y z_0)\theta_z - \frac{1}{2} T_{sv}\theta_z + \theta_z' P_{yz} + \theta_y' P_{yy} \Big] \\
& + \delta\phi[M_y((\theta_y' + \theta_y' u_0')\sin\phi + (\theta_z' + \theta_z' u_0')\cos\phi) + M_z((\theta_z' + \theta_z' u_0')\sin\phi
\end{aligned}$$

$$
\begin{aligned}
&-(\theta_y' + \theta_y' u_0')\cos\phi) - N\phi'(z_0\theta_z - y_0\theta_y)\sin\phi + N(z_0\theta_z' - y_0\theta_y')\cos\phi \\
&+Q_y((\theta_z - v' + \theta_z u_0')\sin\phi - (\theta_y - w' + \theta_y u_0')\cos\phi) + Q_z((\theta_y - w' + \theta_y u_0')\sin\phi \\
&+(\theta_z - v' + \theta_z u_0')\cos\phi)] + \delta\theta_z'' \frac{1}{2} B\theta_y - \delta\theta_y'' \frac{1}{2} B\theta_z + \delta\phi'[T_{\mathrm{w}} + T_{\mathrm{sv}} + B_1\phi' \\
&+N(\theta_z z_0 - \theta_y y_0)\cos\phi] + \delta\theta' B - \delta\theta T_{\mathrm{w}} \Bigg\} \mathrm{d}x
\end{aligned} \tag{26}
$$

$$
\begin{aligned}
L_{\mathrm{P}} = \int_0^L \Bigg\{ & -q_x\delta u_0 - q_y\delta v - q_z\delta w - b\delta\theta - \delta\theta_z' \frac{1}{2} b\theta_y + \delta\theta_y' \frac{1}{2} b\theta_z \\
&+\delta\theta_z \left[m_z\cos\phi - (m_y + z_0 q_x)\sin\phi + \frac{1}{2} b\theta_y' + \frac{1}{2}\lambda_{mx}\theta_y + \lambda_y\theta_z \right] \\
&+\delta\theta_y \left[m_y\cos\phi + (m_z + y_0 q_x)\sin\phi - \frac{1}{2} b\theta_z' + \frac{1}{2}\lambda_{mx}\theta_z + \lambda_z\theta_y \right] \\
&+\delta\phi[-m_x\cos\phi - (m_z\theta_z + m_y\theta_y)\sin\phi - (m_y + z_0 q_x)\theta_z\cos\phi \\
&+(m_z + y_0 q_x)\theta_y\cos\phi + \sin\phi(\lambda_y + \lambda_z + z_0 q_z + y_0 q_y)] \Bigg\} \mathrm{d}x \\
&+ \Bigg| -\bar{N}\delta u_0 - \bar{Q}_y\delta v - \bar{Q}_z\delta w - \bar{B}\delta\theta - \delta\theta_z' \frac{1}{2}\theta_y\bar{B} + \delta\theta_y' \frac{1}{2}\theta_z\bar{B} \\
&+\delta\theta_z \left[\bar{M}_z\cos\phi - (\bar{M}_y + \bar{N}z_0)\sin\phi + \frac{1}{2}\theta_y'\bar{B} + \theta_z\bar{\lambda}_y + \frac{1}{2}\theta_y\bar{\lambda}_{mx} \right] \\
&+\delta\theta_y \left[\bar{M}_y\cos\phi + (\bar{M}_z + \bar{N}y_0)\sin\phi - \frac{1}{2}\theta_z'\bar{B} + \theta_y\bar{\lambda}_z + \frac{1}{2}\theta_z\bar{\lambda}_{mx} \right] \\
&+\delta\phi[-\bar{M}_x\cos\phi - \sin\phi(\bar{M}_z\theta_z + \bar{M}_y\theta_y) - \cos\phi(\bar{M}_y\theta_z - \bar{M}_z\theta_y \\
&+\bar{N}z_0\theta_z - \bar{N}y_0\theta_y) + \bar{B}_1\sin\phi] \Bigg|_{x=0}^{x=L}
\end{aligned} \tag{27}
$$

where q_x, q_y, q_z, m_x, m_y, m_z, b, λ_y, λ_z, and λ_{mx} are resultants of the applied wall surface tractions as defined in Appendix C. In the same way, $\bar{N}$, $\bar{Q}_y$, $\bar{Q}_z$, $\bar{M}_z$, $\bar{M}_y$, $\bar{B}$, $\bar{M}_x$, $\bar{\lambda}_y$, $\bar{\lambda}_z$, $\bar{\lambda}_{mx}$, and $\bar{B}_1$ are defined in Appendix C and represent the resultants of the applied end tractions.

7. Beam forces

In the above expressions, the following 1D beam forces, in terms of the shell stress resultants, have been defined

$$
\begin{aligned}
&N = \int N_{xx}\mathrm{d}s; \qquad M_Y = \int \left(N_{xx}\bar{Z} + M_{xx}\frac{\mathrm{d}Y}{\mathrm{d}s}\right)\mathrm{d}s;\\
&M_Z = \int \left(N_{xx}\bar{Y} - M_{xx}\frac{\mathrm{d}Z}{\mathrm{d}s}\right)\mathrm{d}s; \qquad Q_Z = \int \left(N_{xs}\frac{\mathrm{d}Z}{\mathrm{d}s} + N_{xn}\frac{\mathrm{d}Y}{\mathrm{d}s}\right)\mathrm{d}s;\\
&Q_Y = \int \left(N_{xs}\frac{\mathrm{d}Y}{\mathrm{d}s} - N_{xn}\frac{\mathrm{d}Z}{\mathrm{d}s}\right)\mathrm{d}s; \qquad T_{\mathrm{w}} = \int (N_{xs}(r-\psi) + N_{xn}l)\mathrm{d}s;\\
&B = \int (N_{xx}\omega_p - M_{xx}l)\mathrm{d}s; \qquad T_{\mathrm{sv}} = \int (N_{xs}\psi - 2M_{xs})\mathrm{d}s
\end{aligned}
\tag{28}
$$

where N corresponds to the axial force, Q_y and Q_z to shear forces, M_y and M_z to bending moments about $\bar{y}$- and $\bar{z}$-axis, respectively, B to the bimoment, T_{w} to the flexural–torsional moment and T_{sv} to the Saint–Venant torsional moment. In addition, the following four high-order stress resultants have been defined:

$$
\begin{aligned}
&B_1 = \int [N_{xx}(Y^2 + Z^2) - 2M_{xx}r]\mathrm{d}s; \qquad P_{yy} = \int \left[N_{xx}\bar{Z}^2 + 2M_{xx}\bar{Z}\frac{\mathrm{d}Y}{\mathrm{d}s}\right]\mathrm{d}s;\\
&P_{zz} = \int \left[N_{xx}\bar{Y}^2 - 2M_{xx}\bar{Y}\frac{\mathrm{d}Z}{\mathrm{d}s}\right]\mathrm{d}s;\\
&P_{yz} = \int \left[N_{xx}\bar{Y}\bar{Z} + M_{xx}\left(\bar{Y}\frac{\mathrm{d}Y}{\mathrm{d}s} - \bar{Z}\frac{\mathrm{d}Z}{\mathrm{d}s}\right)\right]\mathrm{d}s
\end{aligned}
\tag{29}
$$

In expressions (28) and (29), the integration is carried out over the entire length of the mid-line contour.

The relations among the generalized beam forces and the generalized strains characterizing the behavior of the beam are obtained by substituting the expressions (16)–(20) into (23), and the results into (28) and (29). This constitutive law can be expressed in terms of a beam stiffness matrix $[K]$ as defined in Appendix B.

8. The discretized equilibrium problem

The equations of motion (25) are discretized to analyze the behavior of simply supported beams under different load conditions. The displacements are approximated by means of the following functions, which are compatible with the boundary conditions of the beam

$$
\begin{aligned}
&u = u_0\frac{x}{L}; \qquad v = v_0\sin\left(\frac{\pi}{L}x\right); \qquad \theta_z = \theta_{z_0}\cos\left(\frac{\pi}{L}x\right);\\
&w = w_0\sin\left(\frac{\pi}{L}x\right); \qquad \theta_y = \theta_{y_0}\cos\left(\frac{\pi}{L}x\right); \qquad \phi = \phi_0\sin\left(\frac{\pi}{L}x\right);\\
&\theta = \theta_0\cos\left(\frac{\pi}{L}x\right)
\end{aligned}
\tag{30}
$$

Table 1
Materials consider in the numerical applications

Properties	Glass/epoxy (M1)	Graphite/epoxy (M2)
Young's modules (GPa)		
E_1	48.3	144
E_2	19.8	9.65
Shear's modules (GPa)		
$G_{12}=G_{13}$	8.96	4.14
G_{23}	6.19	3.45
Poisson's ratio		
$\nu_{12}=\nu_{13}$	0.27	0.3
ν_{23}	0.60	0.5

where u_0, v_0, w_0, θ_{z_0}, θ_{y_0}, ϕ_0 and θ_0 are the associated displacement amplitudes. Besides, these functions (30) represent the exact solution for the linear analysis of thin-walled beams [13]. In order to solve the variational system (25), Ritz's method is first applied. After integration along the beam length according to the adopted functions for the displacements, a coupled and strongly non-linear algebraic system is obtained. This resulting system has an extremely complicated form and, for this reason, is not presented here. An incremental-iterative method based on the Newton–Rapshon method is employed for solving the non-linear equilibrium equations.

9. Applications and numerical results

In the following numerical results, the shear effect on the thickness $\gamma_{xn}^{(0)}$ has been neglected because its consideration conduces to inaccurate results for thin-walled sections, as explained Piovan [18]. He showed that the inclusion of thickness shear–deformation effect increases erroneously the rigidity instead of flexibilizing the beam behavior. Different cross-sectional shapes, laminate schemes and beam lengths are considered to perform the numerical analysis. Material properties corresponding to S2-glass/epoxy (M1) and AS4/3501 graphite/epoxy (M2) were used (see Table 1). The analyzed cross-sections are shown in Fig. 2.

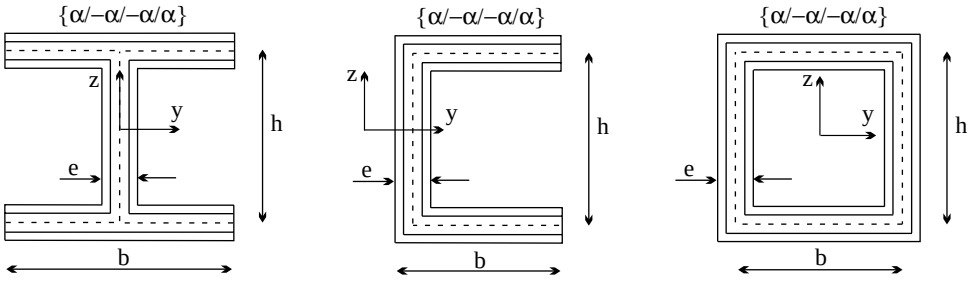

Fig. 2. Analyzed cross-sectional shapes.

10. Flexural–torsional stability analysis

Flexural–torsional buckling and post-buckling of a simply supported beam subjected to a concentrated axial force applied to the centroid is studied. In order to investigate this behavior, the following cases are considered.

10.1. Bisymmetric open cross-section

The example considered is a simply supported bisymmetric-I section whose geometric properties are $L=6$ m, $h=0.6$ m, $b=0.6$ m, $e=0.03$ m. The analyzed material is graphite-epoxy (M2). In this example ($y_0=z_0=0$), the equilibrium equations are non-linear but uncoupled. Therefore, there are three buckling modes corresponding either to bending or to torsion. Taking into account that the flexural mode corresponding to displacement v (y-direction) has the smallest buckling load, the post-buckling curves are presented for the displacement amplitude v_0. The load-deflection curves are shown, in Fig. 3, for different laminate stacking sequences. Moreover, two models are compared: the present theory (model I) and results obtained by neglecting shear flexibility (model II). It is observed from the figures that the post-buckling equilibrium paths are stable and symmetric. The sequence of lamination {0/0/0/0} presents the highest buckling load and also the largest load carrying capacity after buckling. In addition, the shear–deformation effect is considerably more important when this one is used. As may be seen in this case, shear effect reduces the values of the equilibrium path in about 21% with respect to the non-shearable theory. On the other hand, the sequence of lamination {45/−45/−45/45} presents limited margins of post-buckling strength due to its flat shape. Besides, both with

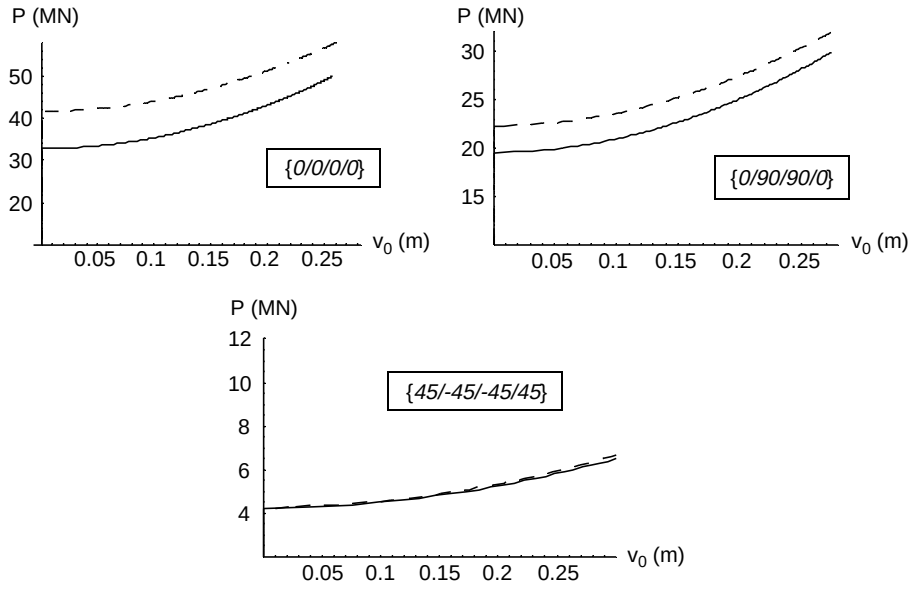

Fig. 3. Post-buckling paths (P,v_0), (–) present theory, (- - -) neglecting shear flexibility.

Table 2
Buckling loads for I-beam subjected to axial force, $L=6$ m ($P\times10^6$ N)

Lamination	Model I	Model II	Cosmos/M
{0/0/0/0}	33.18	42.11	30.02
{0/90/90/0}	19.84	22.57	20.02
{45/−45/−45/45}	4.44	4.45	4.38

and without shear–deformation curves are practically coincident for this last type of lamination.

In Table 2, the linear buckling loads are given for models I and II, and compared with the buckling loads calculated using shell finite elements (Shell4L) from the program Cosmos/M [19]. An acceptable agreement between the present beam theory and Cosmos/M shell finite element is observed. The simply supported thin-walled I-beam was modeled by 120 shell elements and its buckled mode shape is shown in Fig. 4, for a lamination {0/90/90/0}.

10.2. Bisymmetric closed cross-section

In this example, a bisymmetric-Box section is considered with the following geometric properties: $L=6$ m, $h=0.6$ m, $b=0.3$ m, $e=0.03$ m. The analyzed material is the same as the previous example graphite-epoxy (M2). The non-linear behavior of this box beam ($y_0=z_0=0$) subjected to an axial force is similar to the previous example. The load–deflection curves are shown, in Fig. 5, for different laminate stacking sequence. Again, two models are compared: present theory (model I) and results obtained by neglecting shear flexibility (model II). The post-buckling equilibrium paths are stable and symmetric. The beam with unidirectional fibers shows the stiffest post-buckling behavior and then the highest buckling load with respect to the other laminations. In addition, the shear–deformation effect is considerably more important for this beam. For the sequence of lamination {45/−45/−45/45}, there is no influence of the shear–deformation and its additional load carrying capacity after buckling is limited.

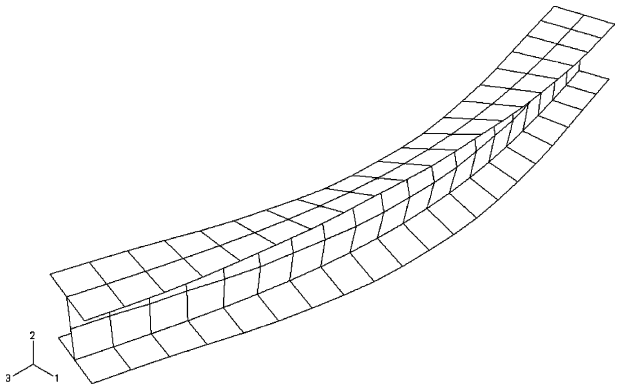

Fig. 4. Buckling mode for a beam I under an axial load, {0/90/90/0}.

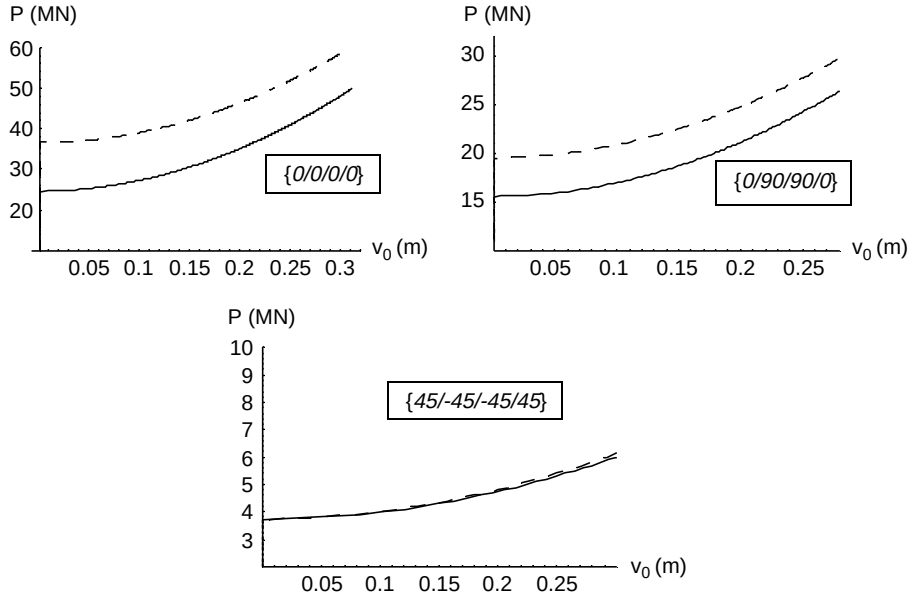

Fig. 5. Post-buckling paths (P,v_0), (–) present theory, (- - -) neglecting shear flexibility.

In Table 3, the buckling loads of the present study are given for models I and II, and compared with the buckling loads calculated using shell finite elements (Shell4L) from the program Cosmos/M. An acceptable agreement between the present beam theory and Cosmos/M shell finite element is observed, while results obtained by neglecting shear flexibility are inaccurate for the lamination {0/0/0/0} and {0/90/90/0}. The simply supported thin-walled Box-beam was modeled by 160 shell elements and its flexural buckling mode shape is shown in Fig. 6, for a lamination {45/−45/−45/45}.

10.3. Monosymmetric cross-section

The considered example is a monosymmetric channel section, the geometric properties are $L=6$ m, $h=0.6$ m, $b=0.6$ m, $e=0.03$ m. The analyzed material is graphite-epoxy (M2). In this case ($z_0=0$), the equilibrium equations corresponding to y-direction (v transversal displacement) are, therefore, uncoupled. Thus, the buckling modes can correspond either to bending in y-direction (v) or to flexural–torsional mode (w and ϕ). For the cross-section analyzed, the flexural–torsional mode presents the smallest buckling

Table 3
Buckling loads for Box-beam, $L=6$ m ($P\times 10^6$ N)

Lamination	Model I	Model II	Cosmos/M
{0/0/0/0}	24.91	37.41	21.23
{0/90/90/0}	15.80	20.05	14.54
{45/−45/−45/45}	3.88	3.89	4.01

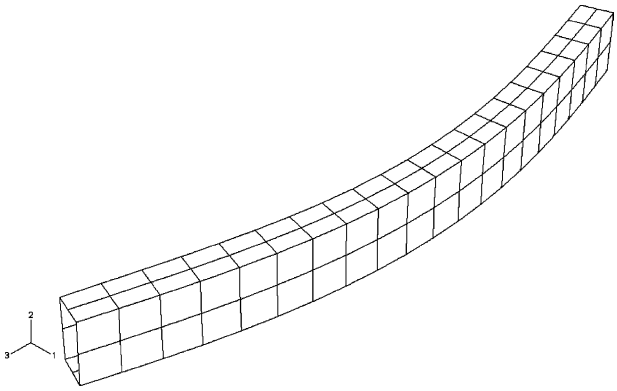

Fig. 6. Buckling mode for a box beam under an axial load, {45/−45/−45/45}.

load. The load–twisting curves are shown in Fig. 7, for different laminate stacking sequence, with and without shear flexibility consideration. The post-buckling equilibrium paths are stable and symmetric. The shear–deformation effect continues being more significant for the lamination {0/0/0/0}and insignificant for the lamination {45/−45/−45/45}. The sequence of lamination {0/0/0/0} has the highest buckling load and the largest additional load carrying capacity after buckling. In Fig. 8, the initial post-buckling paths of the amplitude displacements u_0, w_0 and θ_{y_0} are shown, for a sequence of lamination {0/0/0/0} and considering the models I and II.

In Table 4, the buckling loads of the present study are given for model I and II, and compared with the buckling loads calculated using shell finite elements (Shell4L) from the

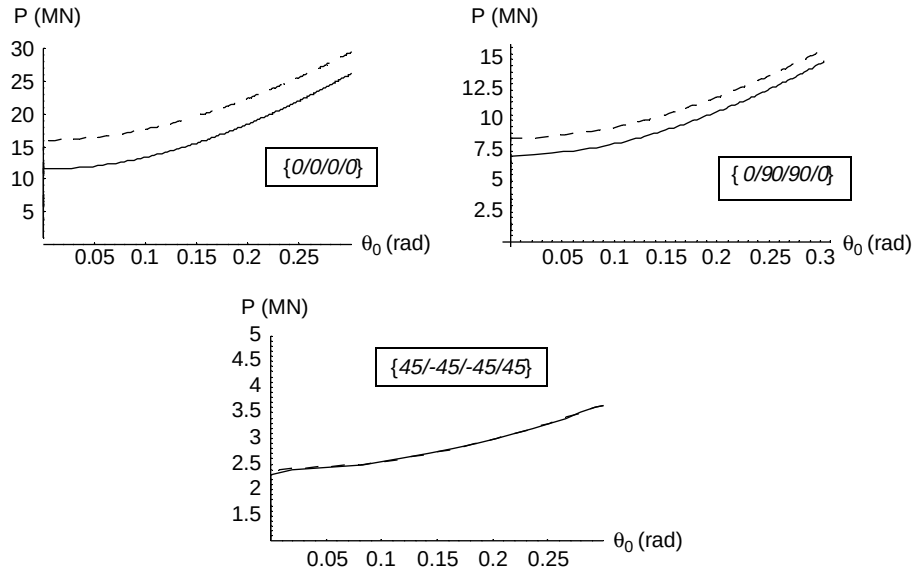

Fig. 7. Post-buckling paths (P,ϕ_0), (–) present theory, (- - -) neglecting shear flexibility.

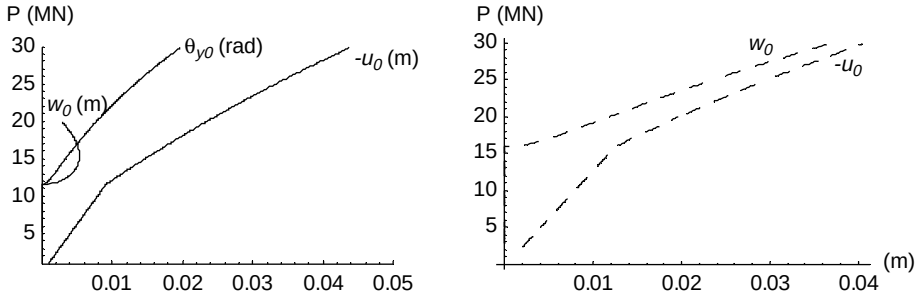

Fig. 8. Post-buckling paths, (–) present theory, (- - -) neglecting shear flexibility.

Table 4
Buckling loads for channel-beam, $L=6$ m ($P\times 10^6$ N)

Lamination	Model I	Model II	Cosmos/M
{0/0/0/0}	11.79	16.23	11.20
{0/90/90/0}	7.37	8.78	7.31
{45/−45/−45/45}	2.61	2.61	2.83

program Cosmos/M. An acceptable agreement between the present beam theory and Cosmos/M shell finite element is observed. The simply supported thin-walled channel-beam is modeled by 120 shell elements and its flexural–torsional buckling mode shape is shown in Fig. 9, for a lamination {45/−45/−45/45}.

10.4. The case of close buckling loads for monosymmetric sections

The considered example is a simply supported channel section subjected to a concentrated axial force applied to the centroid. The geometric properties are $h=0.6$ m, $b=0.3$ m, $e=0.03$ m, and the analyzed material is Glass-epoxy (M1). For this channel section ($z_0=0$), the buckling loads corresponding to the flexural mode (v) and flexural–torsional mode (w and ϕ), coincide for a particular beam length. The variation of the

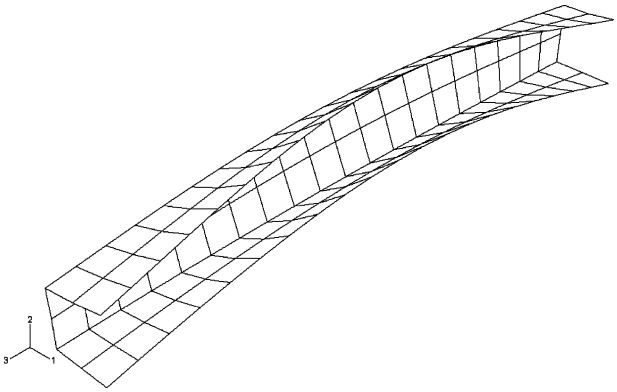

Fig. 9. Buckling mode for a channel beam under an axial load, {45/−45/−45/45}.

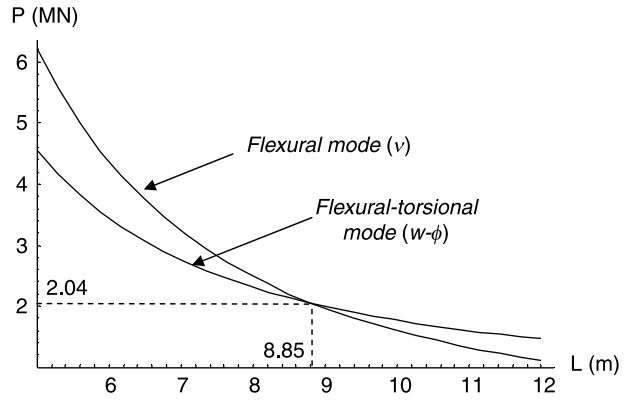

Fig. 10. Buckling load variation with the length, lamination {0/0/0/0}.

buckling loads for both modes is shown as a function of the beam length L in Fig. 10, and for a lamination sequence {0/0/0/0}. As it is clearly shown, the buckling loads coincide for $L=8.85$ m. The buckling mode is flexural for length $L>8.85$ m and is flexural–torsional for less than this value.

In linear stability and design practice, only the smallest buckling load is considered. In post-buckling behavior, when a structure presents two close buckling loads, their interaction must be accounted for. The initial post-buckling path of the channel section previously investigated is shown in Fig. 11. The post-buckling equilibrium paths are stable

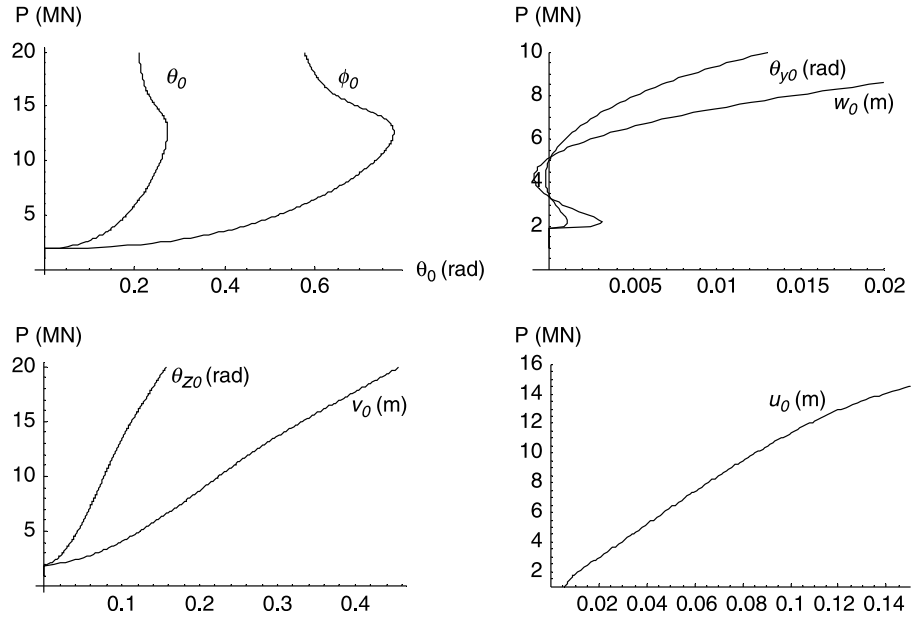

Fig. 11. Post-buckling paths for a channel-beam, {0/0/0/0}, $L=8.85$ m.

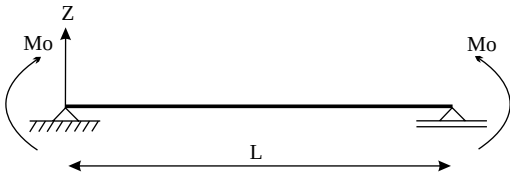

Fig. 12. Simply supported beam subjected to uniform moment.

and symmetric. In particular, load–twisting and warping curves (the upper-left curve) are initially flat and then suddenly stiffen. On the other hand, the secondary paths corresponding to the displacement amplitudes v_0 and θ_{z_0} (the bottom-left curve) show a stiffer behavior in comparison with the ones corresponding to the displacement amplitudes w_0 and θ_{y_0} (the upper-right curve).

11. Lateral stability analysis

When the beam is loaded in the plane the symmetry this initially deflects. However, at a certain level of the applied load, the beam may buckle laterally, while the cross-sections of the beam rotate simultaneously about the beam's axis. This phenomenon is called lateral buckling, and the value of the load at which buckling occurs is the critical load. The initial deflection corresponds to the pre-buckling state, also called 'the fundamental state'. When the buckling load is reached, the behavior of the beam is flexural–torsional. In order to investigate the non-linear lateral stability of three-dimensional beams, we consider a simply supported beam subjected to concentrated end moments, concentrated forces, or uniformly distributed load.

11.1. Simply supported I-beam subjected to uniform moments

A simply supported I-beam subjected to uniform bending moment is considered (with end moments Mo applied about its major axis) as shown in Fig. 12. The geometric

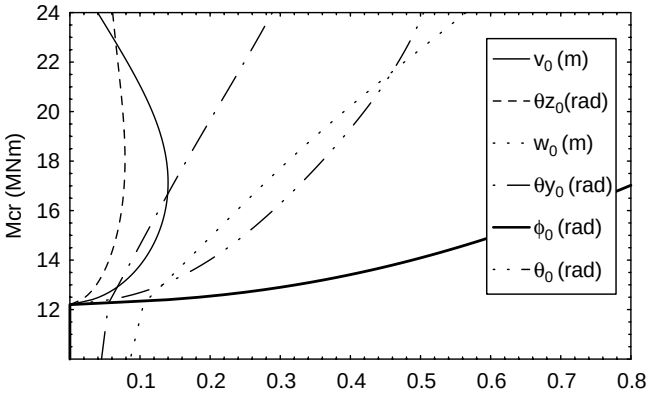

Fig. 13. Lateral post-buckling paths, {0/0/0/0}, $L=6$ m.

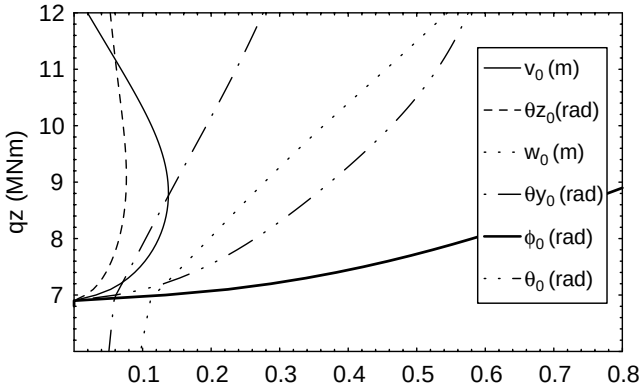

Fig. 14. Lateral post-buckling paths, {0/90/90/0}, $L=6$ m.

properties are $h=0.6$ m, $b=0.6$ m, $e=0.03$ m, and the analyzed material is graphite-epoxy (M2). The equilibrium equations are completely coupled. The initial post-buckling paths of the amplitude displacements v_0, θ_{z_0}, w_0, θ_{y_0}, ϕ_0 and θ_0 are shown in Figs. 13–15, for a beam length $L=6$ m and lamination sequence {0/0/0/0}, {0/90/90/0} and {45/−45/−45/45}, respectively. The post-buckling equilibrium paths are stable and symmetric. We observe that the initial post-buckling behavior is similar for the different sequence of lamination analyzed. The lamination {0/0/0/0} presents the highest buckling load and the largest additional load carrying capacity after buckling. On the other hand, the lamination {45/−45/−45/45} presents the lowest critical load and the greatest pre-deflection w_0 (pre-buckling state). The load–twisting curves are shown in Fig. 16, for different laminate stacking sequence and $L=6$ m, considering two models: present theory (model I) and a non-shearable model (model II). The shear–deformation effect decreases considerably the values of the equilibrium path curves when the lamination {0/0/0/0} is used, while this effect has no influence for the lamination {45/−45/−45/45}. Again, the load–twisting curves for a laminate stacking sequence {0/0/0/0} are shown in Fig. 17, but now considering three different beam lengths. It is observed from Fig. 16 that the influence

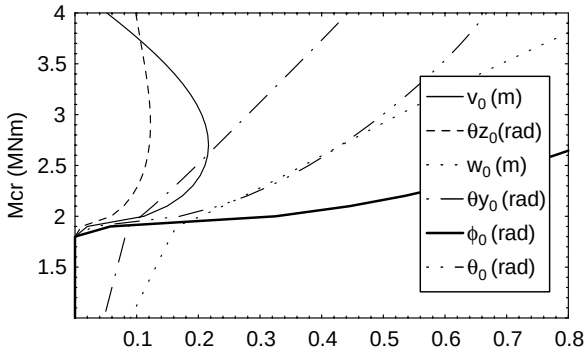

Fig. 15. Lateral post-buckling paths, {45/−45/−45/45}, $L=6$ m.

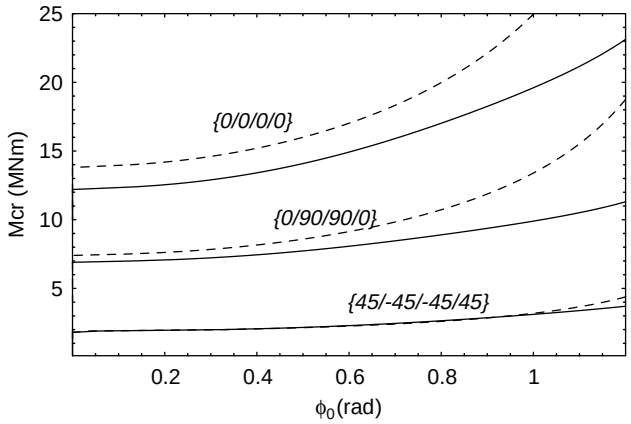

Fig. 16. Post-buckling paths (P,ϕ_0), (–) present theory, (- - -) neglecting shear flexibility.

of shear–deformation is more significant on the post-buckling paths as the beam length decreases. On the other hand, the margins of post-buckling strength are smaller as the beam length increases.

Table 5 shows the buckling moments considering both the linear buckling behavior (classical linear theory [1,20]) and the present theory (geometrically non-linear theory). In the former case, buckling is assumed to be independent of the pre-buckling deflections. As can be seen, the discrepancy between the present buckling moments (considering pre-buckling deflections) and the linear buckling moments is remarkable. The buckling moments computed with the linear stability analysis show a very conservative behavior compared with those computed with the non-linear stability. The influence of the non-linear deflection on the critical loads remains important for the different laminate stacking sequences and beam lengths.

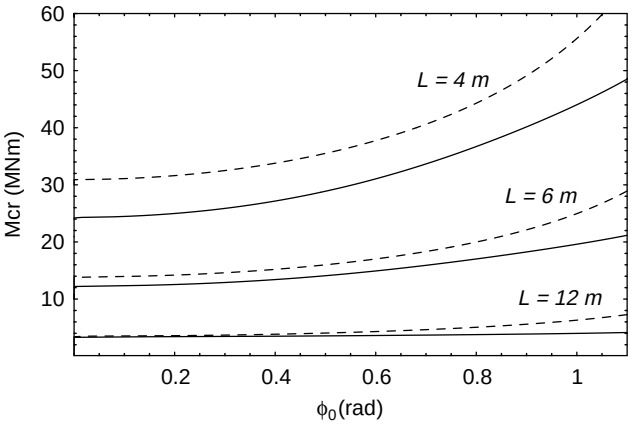

Fig. 17. Post-buckling paths (P,ϕ_0), (–) present theory, (- - -) neglecting shear flexibility.

Table 5
Buckling loads for I-beam subjected to end moments, (Mo$\times 10^6$ N m)

L (m)	Buckling analysis	{0/0/0/0}	{0/90/90/0}	{45/−45/−45/45}
4	Non-linear	26.82	15.96	4.23
	Linear	22.61	13.44	3.55
6	Non-linear	13.53	7.71	2.19
	Linear	11.42	6.51	1.85
12	Non-linear	3.92	2.12	0.85
	Linear	3.21	1.79	0.72

11.2. Simply supported I-beam subjected to distributed load

In this example, a simply supported I-beam under distributed load is considered for three load positions, as shown in Fig. 18. The load can be applied to the top flange (case a), on the shear center (case b), and to the bottom flange (case c). Attention is focused on the importance of the load height parameter effect on the buckling and post-buckling behavior. The geometrical and material properties are the same as the previous example. The load–twisting curves are shown in Fig. 19, for a beam length $L=6$ m and different laminate stacking sequence. The beam behavior is reported for the three loads heights. The post-buckling equilibrium paths are stable and symmetric. The bifurcation point depends on the load height parameter. We observe that the beam resistance to lateral buckling is larger when the loads are applied on the bottom flange (case c). In Figs. 20–22, the initial post-buckling paths of the amplitude displacements v_0, θ_{z_0}, w_0, θ_{y_0}, ϕ_0 and θ_0 are shown, for the load applied on the top flange, centroid and bottom flange, respectively. A beam length $L=6$ and a sequence of lamination {0/0/0/0} is considered. It is observed from the figures that the load–twisting and warping curves (ϕ_0 and θ_0) are similar for the different load heights. On the other hand, the load–deflection curves v_0 presents a stiffer behavior when the load is applied on the top flange. In addition, the pre-buckling displacement w_0 is important in all the cases, but it is quite larger when the load is applied on the bottom flange (Fig. 22).

In Table 6, the buckling loads of the present study are compared with results obtained from the linear analysis, for different lamination and considering the three load height cases. In this case, the influence of the non-linear pre-buckling on the buckling loads is notable, and it becomes greater when the load is applied to the bottom flange. This last fact has been also observed in Fig. 22 for the w_0 pre-buckling behavior.

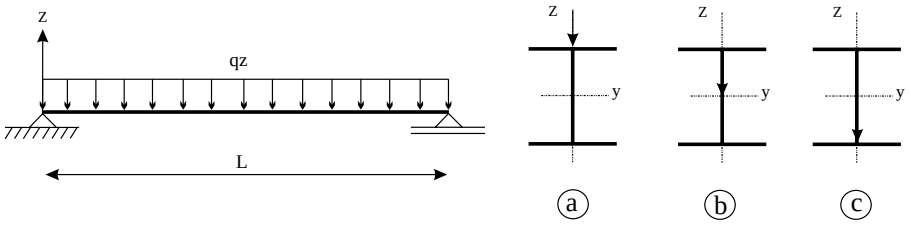

Fig. 18. Different load heights.

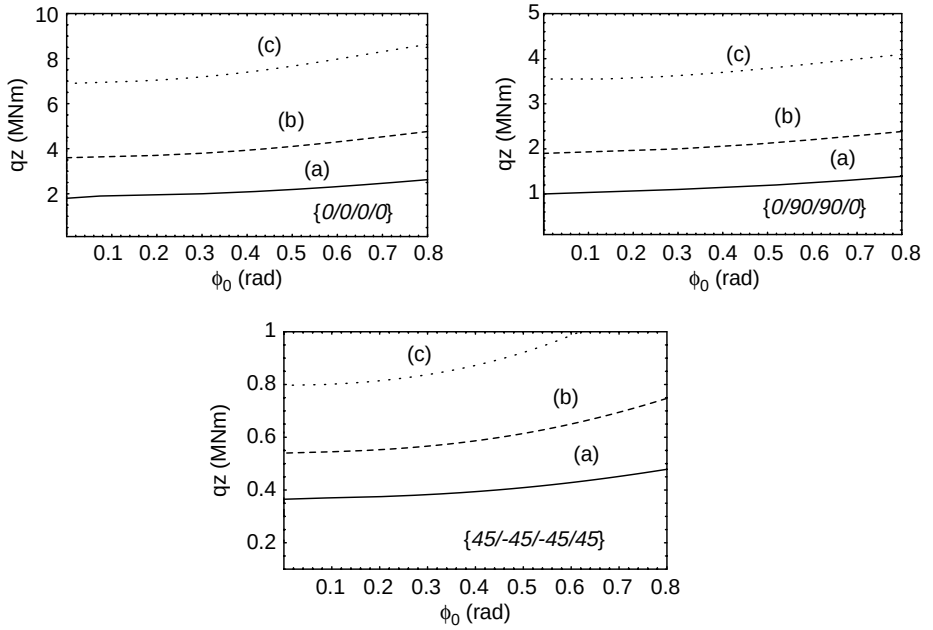

Fig. 19. Lateral post-buckling paths for a I-beam, $L=6$ m.

11.3. Simply supported C-beam subjected to end moments

The example considered here is a simply supported channel beam subjected to equal end moments Mo applied about its major axis, as shown in Fig. 12. The geometric properties are $h=0.6$ m, $b=0.3$ m, $e=0.03$ m. The analyzed material is graphite-epoxy (M2). The initial post-buckling curves are shown in Figs. 23–25, for a beam length $L=6$ m and for the laminate stacking sequences {0/0/0/0}, {0/90/90/0} and {45/−45/−45/45}, respectively. Figs. show that the post-buckling equilibrium paths are stable and

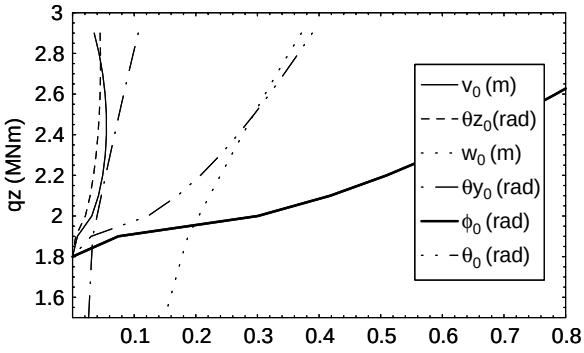

Fig. 20. Post-buckling paths, load on top flange, {0/0/0/0}, $L=6$ m.

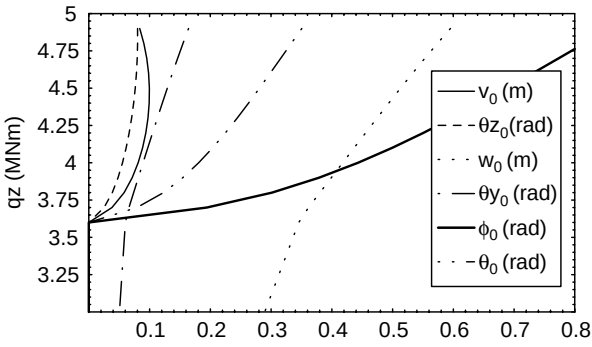

Fig. 21. Post-buckling paths, load on centroid, {0/0/0/0}, $L=6$ m.

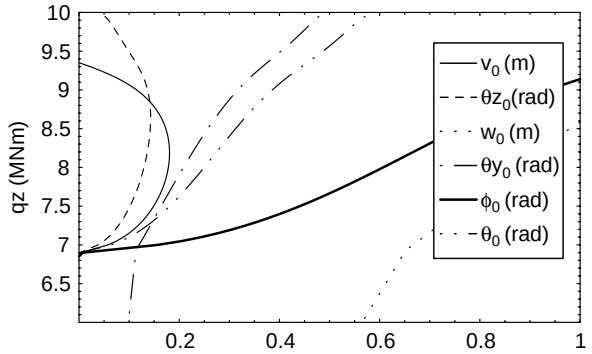

Fig. 22. Post-buckling paths, load on bottom flange, {0/0/0/0}, $L=6$ m.

symmetric. It is observed that the rate of growth of the twisting rotation with load is greater than the analogous rates of growth of in-plane and out-of-plane bending rotations. Besides, the behavior of these last rotations is very similar for the three lamination sequence analyzed.

Table 7 shows the buckling moments considering both the linear buckling analysis (classical theory) and the geometrically non-linear analysis (present theory). In this case,

Table 6
Buckling loads for I-beam subjected to distributed load, $L=6$ m ($q_z \times 10^6$ N m)

Load height	Buckling analysis	{0/0/0/0}	{0/90/90/0}	{45/−45/−45/45}
Top	Non-linear	1.99	1.15	0.38
	Linear	1.75	1.03	0.36
Centroid	Non-linear	3.69	2.03	0.55
	Linear	2.87	1.64	0.46
Bottom	Non-linear	6.82	3.57	0.81
	Linear	4.71	2.61	0.64

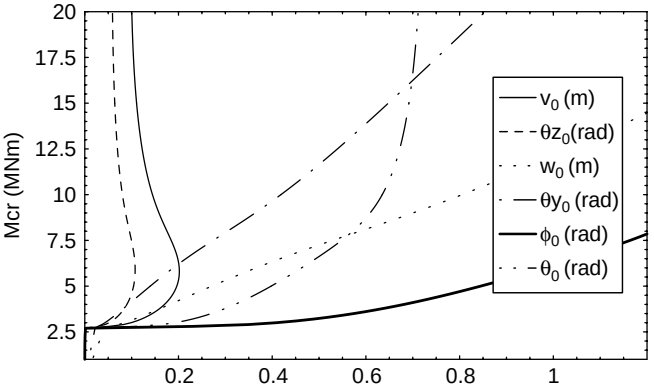

Fig. 23. Lateral post-buckling paths for a channel beam, {0/0/0/0}, $L=6$ m.

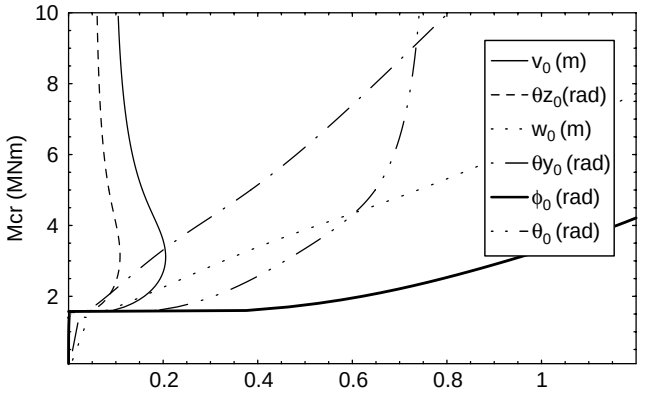

Fig. 24. Lateral post-buckling paths for a channel beam, {0/90/90/0}, $L=6$ m.

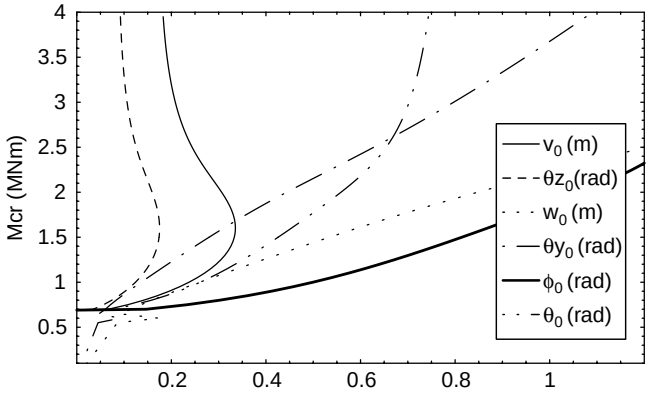

Fig. 25. Lateral post-buckling paths for a channel beam, {45/−45/−45/45}, $L=6$ m.

Table 7
Buckling loads for I-beam subjected to end moments, $L=6$ m ($\text{Mo}\times 10^6$ N m)

Buckling analysis	{0/0/0/0}	{0/90/90/0}	{45/−45/−45/45}
Non-linear	2.67	1.70	0.70
Linear	2.60	1.65	0.68

the agreement between the linear and non-linear buckling loads is very good, because the pre-buckling displacements are negligible.

11.4. Simply supported Box-beam subjected to a concentrated load

A simply supported Box-beam loaded by a transverse force Q_z at the middle of the span is considered for two load positions, as shown in Fig. 26. The load can be applied to the top beam face (case a) and to the bottom beam face (case b). The geometric properties are $L=$ 6 m, $h=0.6$ m, $b=0.3$ m, $e=0.03$ m. The analyzed material is the same as the previous examples graphite-epoxy (M2). In Figs. 27–29, the initial post-buckling paths of the amplitude displacements v_0, θ_{z_0}, w_0, θ_{y_0}, ϕ_0 and θ_0 are shown, considering both load height, and for lamination sequences {0/0/0/0}, {0/90/90/0} and {45/−45/−45/45}, respectively. In this case, the lamination {45/−45/−45/45} presents the greatest resistance to buckling when the load is applied to the upper beam face. Besides, for this last lamination the pre-deflection w_0 is considerably larger, as also the rate of growth of the deflection v_0 with load is greater than the other lamination sequences, in both load conditions. On the other hand, the lamination {0/0/0/0} presents the highest critical load when this load is applied to the bottom beam face.

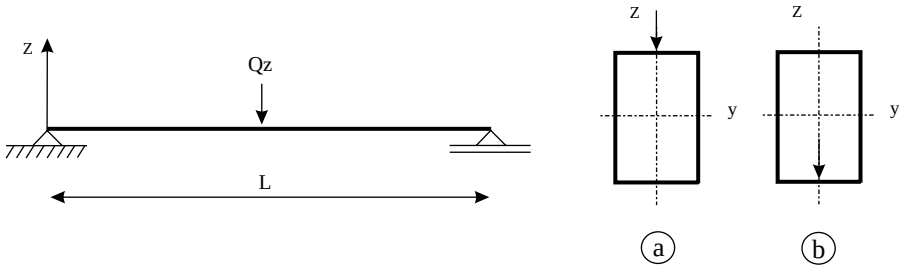

Fig. 26. Box-beam subjected to different load heights.

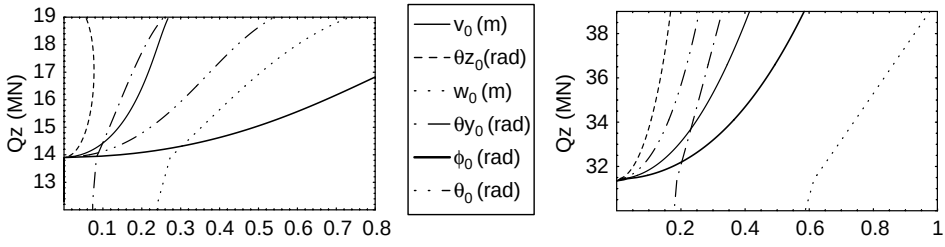

Fig. 27. Post-buckling paths {0/0/0/0}, left curves, load on top; right curves, load on bottom.

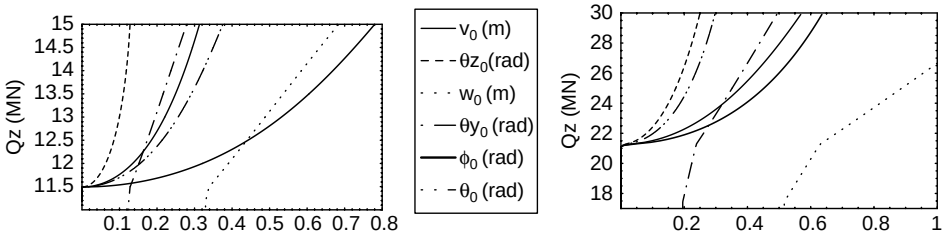

Fig. 28. Post-buckling paths {0/90/90/0}, left curves, load on top; right curves, load on bottom.

The buckling loads of the present study (pre-buckling behavior) are compared with those obtained by the classical linear analysis in Table 8. The influence of the pre-deflection on the buckling loads is very important in this case. It becomes greater when the load is applied to the bottom face. On the other hand, the beam with unidirectional fibres shows a notable difference in the pre-buckling effect when the load position is changed (as can also be observed in the pre-buckling state, Fig. 27).

12. Conclusions

In this paper, a geometrically non-linear theory of thin-walled composite beams is presented to investigate numerically the buckling and post-buckling behavior of simply supported beams. The theory is formulated in the context of large displacements and

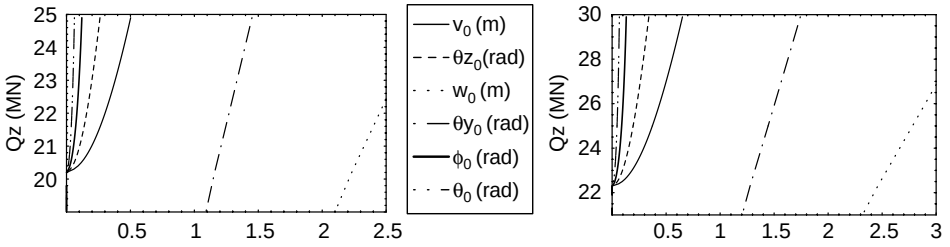

Fig. 29. Post-buckling paths {45/−45/−45/45}, left curves, load on top; right curves, load on bottom.

Table 8
Buckling loads for Box-beam subjected to a concentrated load, $L=6$ m ($Q_z \times 10^6$ N)

Load height	Buckling analysis	{0/0/0/0}	{0/90/90/0}	{45/−45/−45/45}
Top	Non-linear	14.37	11.70	21.60
	Linear	12.11	9.63	15.57
Bottom	Non-linear	31.93	21.27	23.84
	Linear	23.43	15.70	16.76

rotations, through the adoption of a shear–deformable displacement field (accounting for bending and warping shear) considering moderate bending rotations and large twist. The beam model is valid for arbitrary cross-sections, either open or closed. Based on the Ritz's method, an algebraic system is obtained and then solved by an incremental Newton–Raphson algorithm.

From the numerical examples studied, it is found that the agreement between the non-linear buckling loads of the present study and the linear buckling loads obtained with the classical theory are very good when the pre-buckling displacements are small. However, for cases with large pre-buckling displacements, the buckling loads obtained by means of the classical linear theory are very conservative. Thus, when the pre-buckling displacements are not negligible, a non-linear buckling analysis may be required for reliable solutions. From the analysis of laterally loaded beams, it has been established that the buckling loads and the pre-buckling behavior is highly dependent on the load height parameter. On the other hand, the post-buckling curves of the beam showed a stable and symmetric behavior in all the cases analyzed.

Moreover, the shear–deformation effect has been investigated, showing a significant influence for certain laminations, in fact when the beam presents longitudinal fibers. The shear–deformation may significantly decrease the buckling loads and the values of the equilibrium path (post-buckling) of short beams.

Finally, in future works we will extend the application of the present model, for analyzing beams with different boundary conditions.

Acknowledgements

The present study was sponsored by Secretaría de Ciencia y Tecnología, Universidad Tecnológica Nacional, and by CONICET.

Appendix A

The following displacement field corresponding to the one developed by Fraternali and Feo [18], but referred to our Cartesian co-ordinate system is given by (see Fig. 1):

$$
\begin{aligned}
u_x &= u_0 - v'\bar{y} - w'\bar{z} + \phi v' z - \phi w' y + \omega\left[\phi' - \frac{1}{2}(w''v' - w'v'')\right] \\
u_y &= v - \phi z + \frac{1}{2}(-\phi^2 y - v'^2\bar{y} - v'w'\bar{z}) \\
u_z &= w + \phi y + \frac{1}{2}(-\phi^2 z - w'^2\bar{z} - v'w'\bar{y})
\end{aligned}
\tag{A1}
$$

This last is based on the principle of semi-tangential rotation defined by Argyris [21] to avoid the difficulty due to the non-commutative nature of rotations. A remarkable characteristic of this displacement field is the calculation of the warping function carried

out on the bases of two assumptions:

$$\varepsilon_{xn} = 0; \qquad \varepsilon_{xs}|_{n=0} = 0 \tag{A2}$$

Finally, these last assumptions are not taken into account in the expression (4).

Appendix B

The constitutive law for a bisymmetric beam is defined in the following form

$$\{f_g\} = [K]\{\Delta\} \tag{B1}$$

$$\{f_g\} = \begin{bmatrix} N & M_y & M_z & B & Q_y & Q_z & T_w & T_{sv} & B_1 & P_{yy} & P_{zz} & P_{yz} \end{bmatrix}^T \tag{B2}$$

where $\{f_g\}$ is the vector of generalized forces, $\{\Delta\}$ is the vector of the generalized strains. The elements of the symmetric matrix $[K]$ (12×12) are given by the following contour integrals, being null the matrix elements that are not indicated below

$$K_{1,1} = \int \bar{A}_{11}\,\mathrm{d}s; \qquad K_{1,9} = \int \bar{A}_{11}(Y^2+Z^2)\mathrm{d}s; \qquad K_{1,10} = \int \bar{A}_{11}\bar{Z}^2\,\mathrm{d}s;$$

$$K_{1,11} = \int \bar{A}_{11}\bar{Y}^2\,\mathrm{d}s; \qquad K_{1,12} = \int \bar{A}_{11}\bar{Y}\bar{Z}\,\mathrm{d}s; \qquad K_{2,2} = \int(\bar{A}_{11}Z^2 + \bar{D}_{11}Y'^2)\mathrm{d}s;$$

$$K_{2,9} = \int[\bar{A}_{11}\bar{Z}(Y^2+Z^2) - 2\bar{D}_{11}rY']\mathrm{d}s; \qquad K_{2,10} = \int(\bar{A}_{11}\bar{Z}^3 + 2\bar{D}_{11}\bar{Z}Y'^2)\mathrm{d}s;$$

$$K_{2,11} = \int(\bar{A}_{11}\bar{Y}^2\bar{Z} - 2\bar{D}_{11}\bar{Y}Y'Z')\mathrm{d}s; \qquad K_{2,12} = \int[\bar{A}_{11}\bar{Y}\bar{Z}^2 + \bar{D}_{11}(\bar{Y}Y' - \bar{Z}Z')Y']\mathrm{d}s;$$

$$K_{3,3} = \int(\bar{A}_{11}Y^2 + \bar{D}_{11}Z'^2)\mathrm{d}s; \qquad K_{3,9} = \int[\bar{A}_{11}\bar{Y}(Y^2+Z^2) + 2\bar{D}_{11}rZ']\mathrm{d}s;$$

$$K_{3,10} = \int(\bar{A}_{11}\bar{Y}\bar{Z} - 2\bar{D}_{11}\bar{Z}Y'Z')\mathrm{d}s; \qquad K_{3,11} = \int(\bar{A}_{11}\bar{Y}^3 + 2\bar{D}_{11}\bar{Y}Z'^2)\mathrm{d}s;$$

$$K_{3,12} = \int[\bar{A}_{11}\bar{Y}^2\bar{Z} - \bar{D}_{11}(\bar{Y}Y' - \bar{Z}Z')Z']\mathrm{d}s; \qquad K_{4,4} = \int(\bar{A}_{11}\omega_p^2 + \bar{D}_{11}l^2)\mathrm{d}s;$$

$$K_{4,9} = \int[\bar{A}_{11}\omega_p(Y^2+Z^2) + 2\bar{D}_{11}rl]\mathrm{d}s; \qquad K_{4,10} = \int(\bar{A}_{11}\omega_p\bar{Z}^2 - 2\bar{D}_{11}\bar{Z}Y'l)\mathrm{d}s;$$

$$K_{4,11} = \int(\bar{A}_{11}\omega_p\bar{Y} + 2\bar{D}_{11}\bar{Y}Z'l)\mathrm{d}s; \qquad K_{4,12} = \int[\bar{A}_{11}\bar{Y}\omega_p\bar{Z} - \bar{D}_{11}(\bar{Y}Y' - \bar{Z}Z')l]\mathrm{d}s;$$

$$K_{5,5} = \int (\bar{A}_{55} Z'^2 + \bar{A}_{66} Y'^2) \mathrm{d}s; \qquad K_{5,6} = \int (\bar{A}_{66} - \bar{A}_{55}) Z' Y' \, \mathrm{d}s;$$

$$K_{5,7} = \int [\bar{A}_{66} Y' (r - \psi) - \bar{A}_{55} Z' l] \mathrm{d}s; \qquad K_{5,8} = \int \bar{A}_{66} \psi Y' \, \mathrm{d}s;$$

$$K_{6,6} = \int (\bar{A}_{55} Y'^2 + \bar{A}_{66} Z'^2) \mathrm{d}s; \qquad K_{6,7} = \int [\bar{A}_{66} Z' (r - \psi) + \bar{A}_{55} Y' l] \mathrm{d}s;$$

$$K_{6,8} = \int \bar{A}_{66} \psi Z' \, \mathrm{d}s; \qquad K_{7,7} = \int [\bar{A}_{66} (r - \psi)^2 + \bar{A}_{55} l^2] \mathrm{d}s;$$

$$K_{7,8} = \int \bar{A}_{66} \psi (r - \psi) \mathrm{d}s; \qquad K_{8,8} = \int (\bar{A}_{66} \psi^2 + 4 \bar{D}_{66}) \mathrm{d}s;$$

$$K_{9,9} = \int [\bar{A}_{11} (Y^2 + Z^2)^2 + 4 \bar{D}_{11} r^2] \mathrm{d}s;$$

$$K_{9,10} = \int [\bar{A}_{11} (Y^2 + Z^2) \bar{Z}^2 - 4 \bar{D}_{11} \bar{Z} Y' r] \mathrm{d}s;$$

$$K_{9,11} = \int [\bar{A}_{11} (Y^2 + Z^2) \bar{Y}^2 + 4 \bar{D}_{11} \bar{Y} Z' r] \mathrm{d}s;$$

$$K_{9,12} = \int [\bar{A}_{11} (Y^2 + Z^2) \bar{Y} \bar{Z} - 2 \bar{D}_{11} (\bar{Y} Y' - \bar{Z} Z') r] \mathrm{d}s;$$

$$K_{10,10} = \int (\bar{A}_{11} \bar{Z}^4 + 4 \bar{D}_{11} \bar{Z}^2 Y'^2) \mathrm{d}s;$$

$$K_{10,11} = \int (\bar{A}_{11} \bar{Z}^2 \bar{Y}^2 - 4 \bar{D}_{11} \bar{Z} Y' \bar{Y} Z') \mathrm{d}s; \tag{B3}$$

$$K_{10,12} = \int [\bar{A}_{11} \bar{Z}^3 \bar{Y} + 2 \bar{D}_{11} (\bar{Y} Y' - \bar{Z} Z') \bar{Z} Y'] \mathrm{d}s;$$

$$K_{11,11} = \int (\bar{A}_{11} \bar{Y}^4 - 4 \bar{D}_{11} \bar{Y}^2 Z'^2) \mathrm{d}s;$$

$$K_{10,12} = \int [\bar{A}_{11} \bar{Y}^3 \bar{Z} - 2 \bar{D}_{11} (\bar{Y} Y' - \bar{Z} Z') \bar{Y} Z'] \mathrm{d}s;$$

$$K_{12,12} = \int [\bar{A}_{11} \bar{Z}^2 \bar{Y}^2 + \bar{D}_{11} (\bar{Y} Y' - \bar{Z} Z')^2] \mathrm{d}s;$$

where

$$Y' = \frac{\mathrm{d}Y}{\mathrm{d}s}; \qquad Z' = \frac{\mathrm{d}Z}{\mathrm{d}s}; \tag{B4}$$

Appendix C

The resultants of the applied wall surface tractions appearing in (27) are defined below:

$$
\begin{aligned}
&q_x = \int \bar{q}_x \,\mathrm{d}s + \iint \bar{f}_x \,\mathrm{d}s\mathrm{d}n \qquad q_y = \int \bar{q}_y \,\mathrm{d}s + \iint \bar{f}_y \,\mathrm{d}s\mathrm{d}n \\
&q_z = \int \bar{q}_z \,\mathrm{d}s + \iint \bar{f}_z \,\mathrm{d}s\mathrm{d}n \qquad b = \int \bar{q}_x \omega_{\mathrm{p}} \,\mathrm{d}s + \iint \bar{f}_x \omega \,\mathrm{d}s\mathrm{d}n \\
&m_z = \int \bar{q}_x \bar{Y} \,\mathrm{d}s + \iint \bar{f}_x \bar{y} \,\mathrm{d}s\mathrm{d}n \qquad m_y = \int \bar{q}_x \bar{Z} \,\mathrm{d}s + \iint \bar{f}_x \bar{z} \,\mathrm{d}s\mathrm{d}n \\
&m_x = \int (\bar{q}_z \bar{Y} - \bar{q}_y \bar{Z}) \mathrm{d}s + \iint (\bar{f}_z \bar{y} - \bar{f}_y \bar{z}) \mathrm{d}s\mathrm{d}n + q_z y_0 - q_y z_0 \\
&\lambda_y = \int \bar{q}_y \bar{Y} \,\mathrm{d}s + \iint \bar{f}_z \bar{y} \,\mathrm{d}s\mathrm{d}n \qquad \lambda_z = \int \bar{q}_z \bar{Z} \,\mathrm{d}s + \iint \bar{f}_z \bar{z} \,\mathrm{d}s\mathrm{d}n \\
&\lambda_{mx} = \int (\bar{q}_y \bar{Z} + \bar{q}_z \bar{Y}) \mathrm{d}s + \iint (\bar{f}_y \bar{z} + \bar{f}_z \bar{y}) \mathrm{d}s\mathrm{d}n
\end{aligned}
\tag{C1}
$$

The resultants of the applied end tractions are:

$$
\begin{aligned}
&\bar{N} = \iint \bar{p}_x \,\mathrm{d}s\mathrm{d}n \qquad \bar{Q}_y = \iint \bar{p}_y \,\mathrm{d}s\mathrm{d}n \qquad \bar{Q}_z = \iint \bar{p}_z \,\mathrm{d}s\mathrm{d}n \\
&\bar{M}_z = \iint \bar{p}_x \bar{y} \,\mathrm{d}s\mathrm{d}n \qquad \bar{M}_y = \iint \bar{p}_x \bar{z} \,\mathrm{d}s\mathrm{d}n \qquad \bar{B} = \iint \bar{p}_x \omega \,\mathrm{d}s\mathrm{d}n \\
&\bar{M}_x = \iint (\bar{p}_z(\bar{y} + y_0) - \bar{p}_y(\bar{z} + z_0)) \mathrm{d}s\mathrm{d}n \qquad \bar{\lambda}_y = \iint \bar{p}_y \bar{y} \,\mathrm{d}s\mathrm{d}n \\
&\bar{\lambda}_z = \iint \bar{p}_z \bar{z} \,\mathrm{d}s\mathrm{d}n \qquad \bar{\lambda}_{mx} = \iint (\bar{p}_y \bar{z} + \bar{p}_z \bar{y}) \mathrm{d}s\mathrm{d}n \\
&\bar{B}_1 = \iint (\bar{p}_y(\bar{y} + y_0) + \bar{p}_z(\bar{z} + z_0)) \mathrm{d}s\mathrm{d}n
\end{aligned}
\tag{C2}
$$

References

[1] Vlasov VZ. Thin Walled Elastic Beams. Jerusalem: Israel Program for Scientific; 1961.

[2] Davalos JF, Qiao P. Analytical and experimental study of lateral and distorsional buckling of FRP wide-flange beams. ASCE J Compos Construct 1997;1(4):150–9.

[3] Lin WL, Hsiao KM. Co-rotational formulation for geometric nonlinear analysis of doubly symmetric thin-walled beams. Comput Methods Appl Mech Eng 2001;190:6023–52.

[4] Hsiao KM, Lin WL. A co-rotational finite element formulation for buckling and postbuckling analysis of spatial beams. Comput Methods Appl Mech Eng 2000;188:567–94.
[5] Pi YL, Bradford MA. Effects of approximations in analysis of beams of open thin-walled cross-section. Part II: 3-D non-linear behaviour. Int J Numer Meth Eng 2001;51:773–90.
[6] Mohri F, Azrar L, Potier-Ferry M. Lateral post-buckling analysis of thin-walled open sections beams. Thin Walled Struct 2002;40:1013–36.
[7] Kim MY, Chang SP, Kim SB. Spatial postbuckling analysis of nonsymmetric thin-walled frames. II: geometrically nonlinear FE procedures. J Eng Mech 2001;127(8):779–90.
[8] Bhaskar K, Librescu L. A geometrically non-linear theory for laminated anisotropic thin-walled beams. Int J Eng Sci 1995;33(9):1331–44.
[9] Fraternalli F, Feo L. On a moderate rotation theory of thin-walled composite beams. Compos Part B-Eng 2002;31:141–58.
[10] Barbero EJ. Introduction to Composite Material Design. London: Taylor and Francis Inc.; 1999.
[11] Cortínez VH, Machado SP, Piovan MT. Post-pandeo de vigas compuestas de pared delgada, in: First South-American Congress on Computacional Mechanics,Argentina: Paraná; 2002. p. 1713–1729.
[12] Machado SP, Cortínez VH. Análisis de Post-pandeo lateral de vigas compuestas de pared delgada, in: Mecánica Computacional vol. XXII. Argentina: Bahía Blanca; 2003. p. 523–539.
[13] Cortínez VH, Piovan MT. Vibration and buckling of composite thin-walled beams with shear deformability. J Sound Vib 2002;258(4):701–23.
[14] Sapkás A, Kollár LP. Lateral-torsional buckling of composite beams. Int J Solids Struct 2002;39:2939–63.
[15] Cortínez VH, Rossi RE. Dynamics of shear deformable thin-walled open beams subjected to initial stresses. Revista Internacional de Métodos Numéricos para Cálculo y Diseño en Ingeniería 1998;14(3):293–316.
[16] Krenk S, Gunneskov O. Statics of thin-walled pretwisted beams. Int J Numer Meth Eng 1981;17:1407–26.
[17] Washizu K. Variational Methods in Elasticity and Plasticity. NY, USA: Pergamon Press; 1968.
[18] Piovan MT. Estudio teórico y computacional sobre la mecánica de vigas curvas de materiales compuestos, con sección de paredes delgadas, considerando efectos no convencionales. PhD Thesis. Argentina: Universidad Nacional del Sur; 2003.
[19] User's Manual.: Structural Research Analysis Corporation; 1995.
[20] Timoshenko SP, Gere JM. Theory of Elastic Stability. USA: McGraw-Hill; 1961.
[21] Argyris JH. An excursion into large rotations. Comput Methods Appl Mech Eng 1982;32:85–155.